

# Randomness Determines the Fate of Quantum Criticality in 3D Dirac Semimetals

J. P. Santos Pires,<sup>1,2,\*</sup> B. Amorim,<sup>3</sup> Aires Ferreira,<sup>4</sup> İnanç Adagideli,<sup>5,6</sup> Eduardo R. Mucciolo,<sup>2</sup> and J. M. Viana Parente Lopes<sup>1</sup>

<sup>1</sup>*Centro de Física das Universidades do Minho e Porto, University of Porto, 4169-007 Porto, Portugal*

<sup>2</sup>*Department of Physics, University of Central Florida, Orlando, FL 32816, USA*

<sup>3</sup>*Centro de Física das Universidades do Minho e Porto, University of Minho, 4710-057 Braga, Portugal*

<sup>4</sup>*Department of Physics, University of York, YO10 5DD, York, United Kingdom*

<sup>5</sup>*Faculty of Engineering and Natural Sciences, Sabancı University, Orhanlı-Tuzla, 34956, Turkey*

<sup>6</sup>*Faculty of Science and Technology and MESA+ Institute for Nanotechnology, University of Twente, 7500 AE Enschede, The Netherlands*

Dirac-Weyl semimetals are unique three-dimensional (3D) phases of matter with gapless electrons and novel electrodynamic properties believed to be robust against weak perturbations. Here, we unveil the crucial influence of the disorder statistics and impurity diversity in the stability of incompressible electrons in 3D semimetals. Focusing on the critical role played by rare impurity configurations, we show that the abundance of low-energy resonances in realistic potential landscapes endows rare localized zero-energy modes with statistical significance, thus lifting the nodal density of states. The strong nonperturbative effect here reported converts the 3D Dirac-Weyl semimetal into a compressible metal even at the lowest impurity densities. Our analytical results are validated by high-resolution real-space simulations in record-large 3D lattices with up to 536 million orbitals.

The discovery of Dirac and Weyl semimetals (DWSMs) has provided a rich arena for probing novel gapless phases of matter with unique transport properties and topological features [1]. Several types of gapless systems featuring Dirac or Weyl points in 3D momentum space have been realized [2–4]. The simplest DWSMs exhibit two- or four-fold degenerate linear-band touching points at the Fermi level with isotropic velocities and a possible replication into disjoint momentum-space valleys. Their point-like Fermi surface is protected against band gap opening due to either topological constraints (in Weyl systems with broken time-reversal ( $\mathcal{T}$ ) or inversion symmetries ( $\mathcal{P}$ ) [1]) or crystal symmetries (in  $\mathcal{TP}$ -symmetric Dirac systems [5, 6]). Thus, any clean DWSM is an incompressible electron gas with a quadratically vanishing density of states (DoS). Such a paradigm remains, at least qualitatively, in the interacting case. Although electron-electron interactions renormalize the Fermi velocity (with large- $N$  expansions hinting at marginal Fermi liquid behavior [7, 8]), the nodes' integrity and topology remain robust [9–15].

An outstanding question is whether random on-site potentials ubiquitous in realistic systems (e.g., due to impurities in the crystal lattice) can give way to a compressible diffusive metallic phase with a finite nodal DoS [6, 16–31]. An early result by Fradkin predicted that Dirac nodes are stable in  $d=2+\epsilon$  dimensions, below some critical disorder strength [16]. The robustness of DWSMs against weak random perturbations is best visualized by considering a massless particle moving through a short-ranged random potential of strength  $W$ . Since, near a node, the de Broglie wavelength,  $\lambda = \hbar v/E$ , largely exceeds the disorder correlation length, the central limit theorem applies and the fluctuations around the average potential inside a volume  $\lambda^d$  must scale as  $\delta V \propto W \lambda^{-d/2}$ . In  $d=3$ , the fluctuations vanish as  $E^{3/2}$ , i.e. faster than the band energy

near a node, rendering the semimetal phase stable.

The early field-theoretical point of view has been recently questioned by non-perturbative calculations [19, 23], hinting that 3D gapless phases can become unstable due to the emergence of *zero-energy states* bound to statistically rare regions of the disorder potential landscape. According to this picture, the nodal DoS remains nonzero for arbitrarily weak disorder without any signature of singular behavior. Evidence for avoided quantum criticality (AQC) facilitated by localized nodal eigenstates has been provided by lattice simulations of a 3D Dirac model with uncorrelated on-site disorder [23]. Challenging these findings, Buchhold and coauthors noted that rare events are preceded by scattering resonances which always carry zero spectral weight at a node. Furthermore, as they are only possible for fine-tuned (*'magical'*) impurity configurations, this would imply that the nodal DoS cannot be lifted at variance with the AQC scenario [26, 27]. Their claim is backed by the exact solution of a Weyl node with a spherical impurity. These paradoxical findings have attracted significant attention recently [23, 28, 30, 32] because they question the phase stability of incompressible 3D gapless phases in realistic conditions. Moreover, the driving mechanism for semimetal-to-metal transitions in the phase diagram of dirty 3D DWSMs remains elusive.

In this Letter, we resolve this conundrum by tackling the spherical impurity problem using two complementary theoretical approaches. First, within a continuum model, we argue that an unforeseen non-analytic behavior of scattering phase shifts at the node obstructs the use of Friedel's sum rule (FSR) [26, 27], which we tackle with an energy-level statistics analysis. The puzzling behavior of the phase shifts is explained by the emergence and sudden disappearance of bound states upon tuning the impurity potential across a delicate *'magical value'*. Crucially, our level statistics analysis reveals that rare bound

states are accompanied by a *continuum of low-energy resonances* surrounding the node in realistic material systems displaying a *random diversity* of impurity potentials. Such near-critical impurity configurations give effective statistical weight to ‘*magical*’ impurities, and ultimately endow the node with a finite average DoS. Second, we carry out high-precision numerical calculations in a lattice version of the problem, hosting one or more random impurities. Remarkably, our real-space simulations not only unambiguously demonstrate the destabilization of a 3D DWSM by a diversity of near-critical impurities, but also quantitatively agree with the continuum theory predictions in the dilute impurity regime. These findings provide the missing link between continuum and lattice approaches to the dirty DWSM theoretical puzzle and unambiguously pinpoint the newly unveiled *near-critical impurity* configurations as the driving mechanism for AQC. As discussed below, incompressible 3D semi-metallic phases of matter can be either robust or unstable to weak disorder, depending on the statistics of the underlying random potential fluctuations. We note that subtleties in disordered Dirac systems have a long history [33–37]. For instance, in 2D  $d$ -wave superconductors, there are four low-energy quasiparticle Dirac valleys and scalar impurities are pair-breaking. The latter induce resonances that, in the strong scattering limit, turn into sharp DoS peaks at  $E=0$  (Majorana zero modes) [38, 39].

*Continuum theory.*—We start with the low-energy description of a single-valley 3D DWSM. The free Hamiltonian reads  $\mathcal{H}_0 = v_F \boldsymbol{\alpha} \cdot \mathbf{p}$ , with  $\hbar \equiv 1$ ,  $\alpha^i = \sigma^x \otimes \sigma^i$ ,  $v_F$  the Fermi velocity and  $\mathbf{p} = -i\nabla$  the momentum operator. Here,  $\sigma_i$  ( $i=x,y,z$ ) denote Pauli matrices acting on internal spin space. Introducing a scalar impurity potential in the Hamiltonian breaks translation invariance but, if

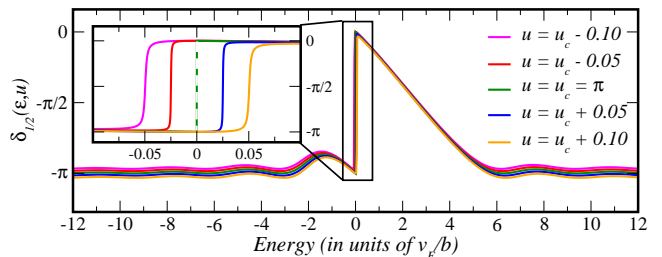


Figure 1. Plot of the energy-dependent phase-shift,  $\delta_{1/2}(\varepsilon, u)$ , in accordance with the prescription  $\delta_j(\varepsilon \rightarrow \pm\infty, u) = -u$ . Several values of  $u$  are plotted around  $u_c = \pi$ .

$\mathcal{U}(\mathbf{r}) = \mathcal{U}(|\mathbf{r}|)$ , rotational symmetry around the impurity center is preserved. Without loss of generality, we consider a spherical well/plateau potential,  $\mathcal{U}(\mathbf{r}) = \lambda\Theta(b - |\mathbf{r}|)$  [19]. The eigenstates of  $\mathcal{H} = \mathcal{H}_0 + \mathcal{U}(|\mathbf{r}|)$  can be written as

$$\Psi_{j,j_z}^\kappa(\mathbf{r}) = \left[ \frac{f_j^\kappa(r)}{r} \Theta_{j,j_z}^{-\kappa}(\hat{\mathbf{r}}), \frac{g_j^\kappa(r)}{r} \Theta_{j,j_z}^\kappa(\hat{\mathbf{r}}) \right]^T. \quad (1)$$

In Eq. (1),  $j \in \{1/2, 3/2, \dots\}$  and  $j_z \in \{-j, -j+1, \dots, j\}$  are the total angular momentum quantum numbers, while  $\kappa = \pm 1$  labels the eigenvalues of  $\mathcal{K} = \gamma^0 \cdot (2\mathbf{L} \cdot \mathbf{S} - 1)$ , i.e.,  $\kappa(j + 1/2)$ . Additionally,  $\Theta_{j,j_z}^\pm(\hat{\mathbf{r}})$  are orthonormal spin-1/2 spherical harmonics and  $f_j^\kappa(r)/g_j^\kappa(r)$  are radial functions. For non-zero energies, the latter are radial spherical waves with phase-shifts introduced by the central potential (see the Supplementary Material (SM) [40] for additional details). In each  $j$ -sector, the scattering phase shifts  $\delta_j$  induced by a spherical well/plateau are obtained by constraining the spinor to be continuous at  $r=b$ . One obtains, after a somewhat lengthy calculation,

$$\tan \delta_j(\varepsilon, u) = \frac{\text{sign}(\varepsilon - u) J_{j+1}(|\varepsilon|) J_j(|\varepsilon - u|) - \text{sign}(\varepsilon) J_j(|\varepsilon|) J_{j+1}(|\varepsilon - u|)}{\text{sign}(\varepsilon) \text{sign}(\varepsilon - u) Y_{j+1}(|\varepsilon|) J_j(|\varepsilon - u|) - Y_j(|\varepsilon|) J_{j+1}(|\varepsilon - u|)}, \quad (2)$$

where  $u \equiv \lambda b/v_F$ ,  $\varepsilon \equiv E b/v_F \neq (0, u)$  and  $J_n(x)(Y_n(x))$  are Bessel functions of 1<sup>st</sup>(2<sup>nd</sup>) kind. Equation (2) is equivalent to that obtained in Refs. [19, 27] for the Weyl equation. This is unsurprising because our  $4 \times 4$  Dirac model is gapless and the impurity is scalar. However, Eq. (2) only defines  $\delta_j(\varepsilon, u)$  modulo  $\pi$ . The ambiguity corresponds, at most, to a global change in the sign of the wavefunction. In order to obtain a unique definition of  $\delta_j(\varepsilon, u)$ , one needs to choose a reference point: as the potential is switched off ( $u \rightarrow 0$ ), the phase shifts vanish across the entire spectrum. A way to guarantee this is to enforce that  $\delta_j(\varepsilon \rightarrow \pm\infty, u) = -u$ , as performed in Refs. [41, 42] [43] (see SM [40] for details). In Fig. 1, we plot  $\delta_{1/2}(\varepsilon)$ , with the previous convention. Clearly, for  $u = u_c = \pi$ , the phase-shift shows a  $\pi$ -discontinuity at  $\varepsilon = 0$ , which marks the

occurrence of zero-energy bound states. For the massless Dirac equation, bound states at  $\varepsilon = 0$  can appear, for particular wells/plateaus, whenever a decoupling of the radial equations for  $f_j^\pm(r > b)/g_j^\pm(r > b)$  occurs [19]. In this case, the admissible (asymptotically decreasing) solutions are simple power-laws,  $g_{j,k}^+(r > b)/f_{j,k}^-(r > b) = \mathcal{B}^\pm r^{-j-1/2}$  and  $f_{j,k}^+(r > b)/g_{j,k}^-(r > b) = 0$ . Such spinors are only continuous at  $r = b$ , if the potential satisfies  $J_j(|u|) = 0$  [40]. Hence, zero-energy states are allowed in a single-impurity Dirac problem provided the parameters are fine-tuned, i.e.  $|\lambda b/v| = u_c^j$  is a root of  $J_j(x)$ . The critical parameters  $\{u_c^j\}$  are dubbed ‘*magical values*’, as they would correspond to rare-regions in a disordered landscape where nonperturbative zero-energy modes are possible [19, 23]. Note that these are true (squared-nor-

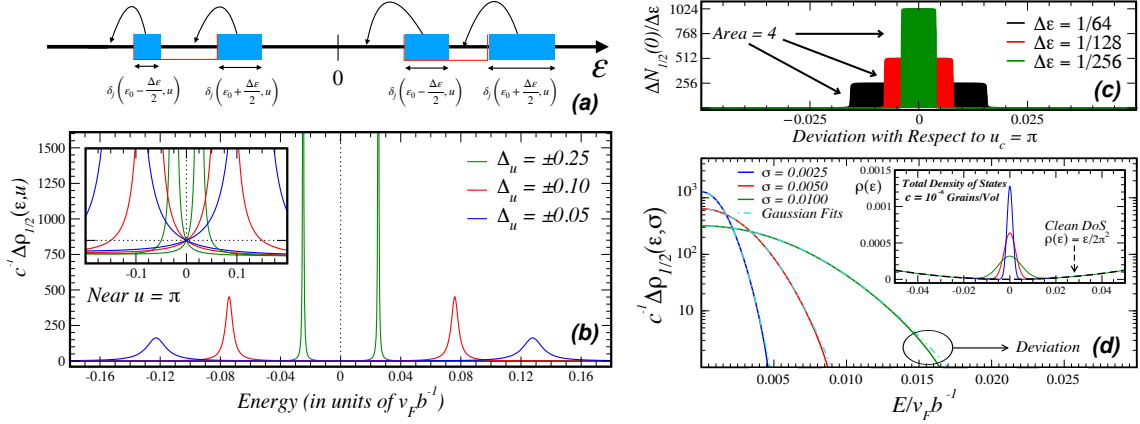


Figure 2. (a) Motion of energy levels triggered by the central impurity. (b) Plots of  $\Delta\rho_{1/2}(\epsilon, u)$  for selected values of  $u$  around  $u_c = \pi$ . The curves were obtained using Eq.(3) with the phase shifts represented in Fig.1. As one approaches  $u_c$ ,  $\Delta\rho_{1/2}(\epsilon)$  takes the form of a low-lying peak, which gets narrower and closer to  $\epsilon = 0$  (roughly conserving the area between zeros). The inset shows that  $\Delta\rho_{1/2}(\epsilon, u)$  is always equal to zero at  $\epsilon = 0$  for any non-critical  $u$ . (c) Depiction of  $\Delta N_{1/2}(\epsilon = 0, \pi) / \Delta\epsilon$  converging towards a distribution  $4\delta(u - \pi)$  as  $\Delta\epsilon \rightarrow 0^+$ . (d) Theoretical prediction for  $\Delta\rho_{1/2}(\epsilon)$  due to dilute spherical impurities with a gaussian diversity of width  $\sigma$  around  $u_c^{1/2} = \pi$ . The inset depicts the total DoS for  $10^{-6}b^{-1}$  impurities/volume.

malizable) impurity bound-states within the Dirac continuum and they have a degeneracy of  $2(2j+1)$ . These bound-states manifest themselves as an  $\epsilon = 0$   $\pi$ -discontinuity in the phase-shifts when the parameter  $u$  crosses a critical value of that angular momentum channel (inset of Fig. 1). This in accord with Levinson's theorem for Dirac particles [41, 42] which states that, given an appropriate convention, the number of bound-states is encapsulated in the phase shifts at zero momentum.

*Impurity-induced change to DoS.*—The change in the DoS induced by an isolated impurity is conventionally calculated using the FSR

$$\Delta\nu(\epsilon, u) = \frac{2}{\pi} \sum_{j=1/2}^{\infty} (2j+1) \frac{\partial \delta_j(\epsilon, u)}{\partial \epsilon}. \quad (3)$$

However, the phase-shift discontinuity caused by the impurity bound-state preclude the direct use of the FSR, an effect so far unnoticed. Therefore, to determine  $\Delta\nu$ , we will use an argument based on counting states within a finite energy window adapted from Friedel's original reasoning [44]. First, we restrict the Dirac fermions to lie inside a finite sphere of radius  $R$ ,  $S_R$ . The hermiticity of  $\mathcal{H}$  is guaranteed if the Hilbert space is restricted to states with vanishing current across the spherical surface,  $\partial S_R$ . That is, to a subspace where any two spinors  $\Psi$  and  $\Phi$ , satisfy  $\oint_{\partial S_R} d\mathbf{S} \cdot [\Psi^\dagger(\mathbf{r}) \boldsymbol{\alpha}_{\mu\nu} \Phi_\nu(\mathbf{r})] = 0$ . In Eq. (1), this is true if  $\cos \delta_j(\epsilon, u) J_j(|\epsilon|R) - \sin \delta_j(\epsilon, u) Y_j(|\epsilon|R) = 0$ . For each angular momentum sector, this condition quantizes the allowed energies levels, which we denote by  $\epsilon_n^j$ . The number of ( $j$ -sector) levels inside the energy window  $[\epsilon_0 - \Delta\epsilon/2, \epsilon_0 + \Delta\epsilon/2]$  is changed by the impurity due to an inwards/outwards migration of levels from regions of width  $\simeq \delta_j(\epsilon \pm \Delta\epsilon/2, u) / R$  (up to  $\mathcal{O}(R^{-2})$ ) near the respective boundaries. This mechanism is illustrated in Fig. 2a. The variation in the number of  $j$ -states inside the probing window is

$$\Delta N_j(\epsilon_0, \Delta\epsilon, u) = \frac{2(2j+1)}{\pi} [\delta_j(\epsilon_0 + \frac{\Delta\epsilon}{2}, u) - \delta_j(\epsilon_0 - \frac{\Delta\epsilon}{2}, u)]. \quad (4)$$

For a finite  $\Delta\epsilon$ , Eq. (4) is accurate in the asymptotic limit  $R \gg 1$  and for  $\epsilon_0 \pm \Delta\epsilon/2 \neq 0$  [40].

Next, we consider the intensive DoS induced by a finite density ( $c$ ) of impurities in a volume  $V$  focusing on single scattering events. The neglect of quantum-coherent scattering by multiple impurities is justified in the dilute regime, where quantum interference corrections are suppressed by a factor of  $1/(k_F l)$  [45, 46], where  $l \propto c^{-1}$  is the mean free path—an important assumption confirmed precisely by our numerical simulations below. Formally, the DoS is obtained by the limiting procedure,  $\Delta\rho(\epsilon_0) = \lim_{\Delta\epsilon \rightarrow 0^+} \lim_{V \rightarrow \infty} [\Delta N(\epsilon_0, \Delta\epsilon, \{u_i\}, V) / V \Delta\epsilon]$ , where  $i$  indexes the impurity and  $\Delta N(\epsilon_0, \Delta\epsilon, \{u_i\}, V)$  is the variation in the total number of states. Assuming that  $\{u_i\}$  are drawn with a probability density  $p(u)$ , the thermodynamic limit then reads

$$\sum_i \frac{\Delta N_j(\epsilon_0, \Delta\epsilon, u_i)}{V} \xrightarrow{V \rightarrow \infty} c \int du p(u) \Delta N_j(\epsilon_0, \Delta\epsilon, u), \quad (5)$$

where  $\Delta N_j(\epsilon_0, \Delta\epsilon, u)$  is given by Eq. (4). The final expression for the DoS variation due to a dilute set of random impurities,  $\Delta\rho(\epsilon_0) = \sum_j \Delta\rho_j(\epsilon_0)$ , is obtained from

$$\Delta\rho_j(\epsilon_0) = c \lim_{\Delta\epsilon \rightarrow 0^+} \int du p(u) \frac{\Delta N_j(\epsilon_0, \Delta\epsilon, u)}{\Delta\epsilon}. \quad (6)$$

The order of limits in Eqs. (5)-(6) is essential. The integration over  $u$  must be done prior to taking the  $\Delta\epsilon \rightarrow 0^+$  limit. This is reminiscent of lattice simulations, where the resolution parameter must be sent to zero only after the thermodynamic limit has been taken (see below). If  $\delta_j(\epsilon, u)$  is differentiable at  $\epsilon = \epsilon_0$ , the  $\Delta\epsilon \rightarrow 0^+$  limit can be safely brought inside the integral, and one obtains  $\Delta\rho_j(\epsilon_0) = c(4j+2) \langle \partial \delta_j(\epsilon, u) / \partial \epsilon |_{\epsilon=\epsilon_0} \rangle_u / \pi$ , where  $\langle f \rangle_u = \int du p(u) f(u)$ , i.e., the familiar FSR. A direct applica-

tion of the FSR [Eq. (3)] was employed in Refs. [26, 27] to determine the DoS in Weyl systems with statistical fluctuations of  $u$  around a critical value  $u_c$ , leading to the conclusion that  $\Delta\rho_j(0) = 0$ . This was inferred from the fact that  $\partial\delta_j(\varepsilon, u)/\partial\varepsilon|_{\varepsilon=0} = 0$  for any  $u \neq u_c^j$ ; see Fig. 2b. Since critical configurations ( $u = u_c^j$ ) have zero statistical measure, the FSR would seemingly imply a vanishing average DoS at  $\varepsilon = 0$ . As shown in the remainder of this Letter, carefully accounting for the limited applicability of the FSR due to the discontinuity in  $\delta_j(\varepsilon, u = u_c)$ , drastically alters the fate of  $\rho(\varepsilon = 0)$  and, with it, the stability of the DWSM.

*Near-critical impurities lift the  $\varepsilon = 0$  DoS.*—Given a statistical distribution of impurities, configurations with a finite concentration of critical impurities do not contribute to the DoS, as the latter involve fine-tuned values of  $u$ , with no statistical significance. However, low-energy resonances due to ‘near-critical’ configurations ( $u \approx u_c^j$ ) provide such a contribution. The phase shifts of such impurities signal the emergence of the zero-energy bound states by a sharp resonance, namely, a quick  $\pi$ -variation of  $\delta_j(\varepsilon)$  as  $u \rightarrow u_c^j$  originated in the valence band, which moves towards  $\varepsilon = 0$  and becomes sharper while always keeping  $\delta_j(0, u) = 0$ . At  $u = u_c$ , the situation is delicate because  $\delta_j(\varepsilon)$  is no longer differentiable at  $\varepsilon = 0$ . In that case, one must work with Eq. (6) directly, and since there is a zero-energy  $\pi$ -discontinuity in the phase shifts, a Dirac- $\delta$  distribution around the  $u_{c,n}^j$  emerges as the limit of plateau functions with a conserved integral equal to 4 (the degeneracy of the  $j = 1/2$  single-impurity bound-states). This limit is depicted in Fig. 2a. An immediate implication is that a DWSM is unstable to dilute random impurities provided  $p(u_c^j) \neq 0$  for some critical  $u_c^j$ .

In Fig. 2d, we plot the change in the  $j = 1/2$  DoS due to a dilute diversity of ‘near-critical impurities’. The diversity is characterized by a gaussian distribution  $p(u) = \exp[-(u - \pi)/2\sigma^2]/\sqrt{2\pi}\sigma$  around  $u_c = \pi$ . The DoS is clearly lifted around  $\varepsilon = 0$ , forming a sharp symmetrical bump. For this diversity model, the peak is gaussian-shaped near its center and the corresponding area is conserved as  $\sigma \rightarrow 0$ . In this limit, a  $4\delta(\varepsilon)$  distribution forms, i.e., all impurities are critical, each having a four-fold degenerate zero-energy bound state.

*Lattice simulations.*—Our prediction for the lifting of the DoS due to near-critical impurities has been based on a continuum model for a single-node Dirac semimetal. However, real Dirac materials and numerical simulations live in the realm of lattice models, featuring several nodes and warped band structures. To validate our previous conclusions, we perform real-space simulations on a simple cubic lattice ( $\mathcal{L}_C$  of parameter  $a$  and linear size  $L$ ) with a four-orbital Hamiltonian derived from the continuum Hamiltonian  $\mathcal{H}$  [22–24], namely,

$$H = \sum_{\mathbf{R} \in \mathcal{L}_C} \left[ \frac{w_F}{2a} \Psi_{\mathbf{R}}^\dagger \cdot \alpha^j \cdot \Psi_{\mathbf{R}+a\mathbf{e}_j} + \frac{\mathcal{U}(\mathbf{R})}{2} \Psi_{\mathbf{R}}^\dagger \cdot \Psi_{\mathbf{R}} + \text{h.c.} \right]. \quad (7)$$

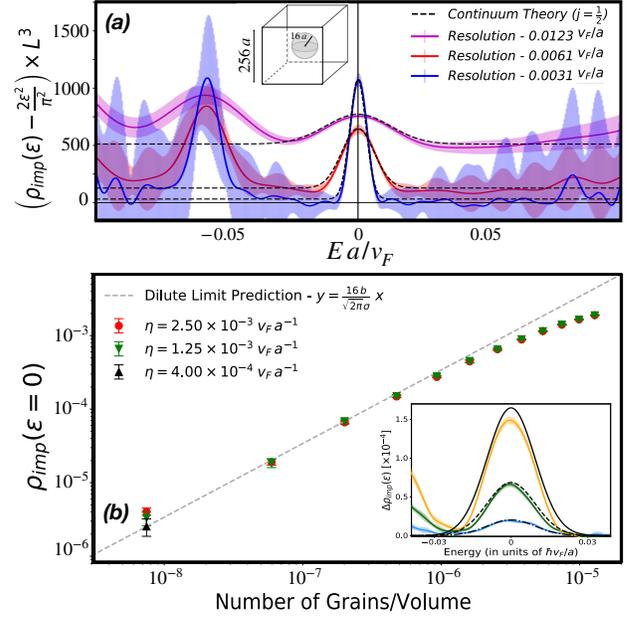


Figure 3. (a) Change in the DoS due to a single impurity of critical strength  $u = \pi v_F a^{-1}$  and radius  $16a$  inside a supercell of  $256^3$  sites. Vertical widths are 95% statistical error bars and the dashed lines are continuum theory predictions. (b) Plot of  $\langle \rho(E=0) \rangle_u$  with several impurities of radius  $16a$  inside the simulated supercell of  $512^3$  sites for different resolutions  $\eta$ . The gray line is the theory prediction in the dilute regime. The inset shows the converged  $\langle \rho(E) \rangle_u$  for three concentrations against the predictions of Fig. 2d (black lines).

The DoS is calculated by means of accurate Chebyshev polynomial expansions of the resolvent operator  $\delta(E - H)$  in very large systems as implemented in the open-source quantum transport code **Quantum KITE** [47]. The energy resolution reads as  $\eta = \pi\Delta E/2M$ , where  $\Delta E$  is the bandwidth of the Hamiltonian matrix and  $M$  is the truncation order of the polynomial expansion [48, 49]. The DoS is obtained from  $\rho(E) = \lim_{\eta \rightarrow 0} \lim_{D \rightarrow \infty} D^{-1} \text{Tr}[\langle \delta_\eta(E - H) \rangle]$ , where  $\langle \dots \rangle$  denotes disorder averaging and  $D = 4L^3$  is the Hilbert space dimension. In order to simulate systems with a vanishing mean level spacing, thereby performing calculations bounded only by  $\eta$ , we randomly sample over twisted boundaries [29, 30]. This approach allowed the DoS to be calculated with unprecedented working spectral resolutions as low as  $\eta \simeq 4 \times 10^{-4} v_F/a$ , whose full convergence requires  $M \approx 30000$  polynomials. Further technical details are given in the SM [40].

Figure 3a shows the average DoS induced by critical impurities,  $\Delta\rho(E) = \rho_{\text{imp}}(E, u = \pi) - 2E^2/\pi^2$ , in the dilute regime. The numerical data is compared with our analytical results [Eq. (6) and discussion thereafter], properly convoluted with gaussian functions of width  $\eta$  to mimic the finite numerical spectral resolution. The lifting of the DoS at the node and the underlying near-critical impurity mechanism is borne out by the spectral calculations, which show excellent quantitative agreement with the continuum theory (Fig. 3a), provided the impurity radius is large enough [40]. In Fig. 3b, we present an analogous

calculation for a system having several impurities inside the supercell. The impurities are placed randomly without superpositions, and strengths drawn from gaussian distributions  $\mathcal{N}(\mu = \pi v_F a^{-1}; \sigma = 0.3v_F/b)$ . The continuum theory prediction for the low-energy bump in the DoS is reproduced in the diluted limit (see inset of Fig. 3b, and the law  $\rho(\varepsilon=0) \propto c$  remains accurate up to  $10^{-6}$  impurities per unit cell. The undershooting for higher concentrations is due to multi-impurity effects, which become more effective as impurities are pushed closer together.

*Outlook.*—We have determined the conditions under which AQC may characterize the phase diagram of a DWSM with short-range impurities. A related, but non-trivial, question concerns the validity of these conclusions when dealing with lattice models having uncorrelated on-site disorder. In the light of our theory, as well as earlier work [23, 28], one reasonably expects the semi-metallic phase to be unstable for unbounded distributions. However, such systems with highly concentrated and atomic-sized impurities (a single-site) are exactly in the regime where lattice results deviate from continuum predictions. Such deviations hint at further subtleties when relating rare-region bound states with the fate of disordered DWSM phases.

We acknowledge support by the Portuguese Foundation for Science and Technology through the Strategic Funding UIDB/04650/2020, projects POCI-01-0145-FEDER-028887 (J.P.S.P., J.M.V.P.L), CEECIND/02936/2017 (B.A.) and grant Nr. PD/BD/142774/2018 (J.P.S.P.). A.F. acknowledges financial support from the Royal Society through a Royal Society University Research Fellowship. The numerical calculations were performed on the Viking Cluster, a High Performance Computing (HPC) facility provided by the University of York. We are grateful for support from the University of York's HPC service and their team. J.P.S.P. is grateful to M. Gonçalves and J.M.B. Lopes dos Santos for discussions, and S.M. João for revising the manuscript.

---

\* Corresponding author: up201201453@fc.up.pt

- [1] N. P. Armitage, E. J. Mele, and A. Vishwanath, *Rev. Mod. Phys.* **90**, 015001 (2018).
- [2] S. Borisenko, Q. Gibson, D. Evtushinsky, V. Zabolotnyy, B. Büchner, and R. J. Cava, *Phys. Rev. Lett.* **113**, 027603 (2014).
- [3] H.-J. Noh, J. Jeong, E.-J. Cho, K. Kim, B. I. Min, and B.-G. Park, *Phys. Rev. Lett.* **119**, 016401 (2017).
- [4] S.-Y. Xu, I. Belopolski, N. Alidoust, M. Neupane, G. Bian, C. Zhang, R. Sankar, G. Chang, Z. Yuan, C.-C. Lee, S.-M. Huang, H. Zheng, J. Ma, D. S. Sanchez, B. Wang, A. Bansil, F. Chou, P. P. Shibayev, H. Lin, S. Jia, and M. Z. Hasan, *Science* **349**, 613 (2015).
- [5] S. M. Young, S. Zaheer, J. C. Y. Teo, C. L. Kane, E. J. Mele, and A. M. Rappe, *Phys. Rev. Lett.* **108**, 140405 (2012).
- [6] B.-J. Yang and N. Nagaosa, *Nat. Comm.* **5**, 4898 (2014).
- [7] J. González, *Phys. Rev. B* **90**, 121107 (2014).
- [8] J. Hofmann, E. Barnes, and S. Das Sarma, *Phys. Rev. B* **92**, 045104 (2015).
- [9] M. Laubach, C. Platt, R. Thomale, T. Neupert, and S. Rachel, *Phys. Rev. B* **94**, 241102(R) (2016).
- [10] J. Carlström and E. J. Bergholtz, *Phys. Rev. B* **97**, 161102(R) (2018).
- [11] J. Carlström and E. J. Bergholtz, *Phys. Rev. B* **98**, 241102(R) (2018).
- [12] W. Witczak-Krempa, M. Knap, and D. Abanin, *Phys. Rev. Lett.* **113**, 136402 (2014).
- [13] B. Roy and S. Das Sarma, *Phys. Rev. B* **94**, 115137 (2016).
- [14] B. Roy, P. Goswami, and V. Juričić, *Phys. Rev. B* **95**, 201102 (2017).
- [15] B. Roy, R.-J. Slager, and V. Juričić, *Phys. Rev. X* **8**, 031076 (2018).
- [16] E. Fradkin, *Phys. Rev. B* **33**, 3263 (1986).
- [17] R. Shindou and S. Murakami, *Phys. Rev. B* **79**, 045321 (2009).
- [18] P. Goswami and S. Chakravarty, *Phys. Rev. Lett.* **107**, 196803 (2011).
- [19] R. Nandkishore, D. A. Huse, and S. L. Sondhi, *Phys. Rev. B* **89**, 245110 (2014).
- [20] S. V. Syzranov, L. Radzihovsky, and V. Gurarie, *Phys. Rev. Lett.* **114**, 166601 (2015).
- [21] B. Sbierski, K. S. C. Decker, and P. W. Brouwer, *Phys. Rev. B* **94**, 220202(R) (2016).
- [22] J. H. Pixley, P. Goswami, and S. Das Sarma, *Phys. Rev. B* **93**, 085103 (2016).
- [23] J. H. Pixley, D. A. Huse, and S. Das Sarma, *Phys. Rev. X* **6**, 021042 (2016).
- [24] J. H. Pixley, D. A. Huse, and S. Das Sarma, *Phys. Rev. B* **94**, 121107(R) (2016).
- [25] S. Syzranov, V. Gurarie, and L. Radzihovsky, *Ann. Phys.* **373**, 694 (2016).
- [26] M. Buchhold, S. Diehl, and A. Altland, *Phys. Rev. Lett.* **121**, 215301 (2018).
- [27] M. Buchhold, S. Diehl, and A. Altland, *Phys. Rev. B* **98**, 205134 (2018).
- [28] K. Ziegler and A. Sinner, *Physical Review Letters* **121**, 166401 (2018).
- [29] M. Gonçalves, P. Ribeiro, E. V. Castro, and M. A. N. Araújo, *Phys. Rev. Lett.* **124**, 136405 (2020).
- [30] J. H. Wilson, D. A. Huse, S. Das Sarma, and J. H. Pixley, *Phys. Rev. B* **102**, 100201(R) (2020).
- [31] K. Kobayashi, M. Wada, and T. Ohtsuki, *Phys. Rev. Research* **2**, 022061 (2020).
- [32] B. Roy, V. Juričić, and S. Das Sarma, *Sci. Rep.* **6**, 32446 (2016).
- [33] W. A. Atkinson, P. J. Hirschfeld, A. H. MacDonald, and K. Ziegler, *Phys. Rev. Lett.* **85**, 3926 (2000).
- [34] P. J. Hirschfeld and W. A. Atkinson, *J. Low Temp. Phys.* **126**, 881 (2002).
- [35] C. Pépin and P. A. Lee, *Phys. Rev. B* **63**, 054502 (2001).
- [36] I. Adagideli, D. E. Sheehy, and P. M. Goldbart, *Phys. Rev. B* **66**, 140512 (2002).
- [37] A. Altland, B. Simons, and M. Zirnbauer, *Physics Reports* **359**, 283 (2002).
- [38] A. V. Balatsky, M. I. Salkola, and A. Rosengren, *Phys. Rev. B* **51**, 15547 (1995).
- [39] I. Adagideli, P. M. Goldbart, A. Shnirman, and A. Yazdani, *Phys. Rev. Lett.* **83**, 5571 (1999).
- [40] “See supplemental material.”

- [41] Z.-Q. Ma and G.-J. Ni, *Phys. Rev. D* **31**, 1482 (1985).
- [42] Z.-Q. Ma, *Jour. Phys. A: Math. Gen.* **39**, R625 (2006).
- [43] As  $\varepsilon \rightarrow \pm\infty$ , one has  $\tan \delta_j(\varepsilon, u) \rightarrow -\tan u$ . This differs from the limiting behavior introduced in Ref. [41],  $\lim_{\varepsilon \rightarrow \pm\infty} \delta_j(\varepsilon, u) = \mp u$ . The difference comes from the  $\text{sign}(\varepsilon)$  factors introduced when defining the radial scattering wavefunctions [see Eqs. (14a)-(15d) of the SM [40]].
- [44] J. Friedel, *The London, Edinburgh, and Dublin Philosophical Magazine and Journal of Science* **43**, 153 (1952).
- [45] A. Altland and B. Simons, *Condensed Matter Field Theory* (Cambridge University Press).
- [46] M. Millettari and A. Ferreira, *Phys. Rev. B* **94**, 134202 (2016).
- [47] S. M. João, M. Anđelković, L. Covaci, T. G. Rappoport, J. M. Viana Parente Lopes, and A. Ferreira, *R. Soc. open sci.* **7**, 191809 (2020).
- [48] A. Weiße, G. Wellein, A. Alvermann, and H. Fehske, *Rev. Mod. Phys.* **78**, 275 (2006).
- [49] A. Ferreira and E. R. Mucciolo, *Phys. Rev. Lett.* **115**, 106601 (2015).

# Supplemental Material

## 1. Spherical Dirac States

Here, we provide technical details on the calculations leading from the Dirac eigenvalue problem in the presence of a single central scalar potential —  $\mathcal{H} = \mathcal{H}_0 + \mathcal{U}(|\mathbf{r}|)$ . These results form the theoretical foundation for the main results presented in this Letter. Since the methods employed are scattered around existing literature [19, 41, 42], we provide a detailed description of procedures to make the discussion self-contained.

### a. Derivation of the Radial Dirac Equations and Radial Eigenstates

The eigenvalue problem for an independent Dirac particle in the presence of a central potential corresponds to finding the solutions of

$$\mathcal{H}_{\mu\nu}\Psi_\nu(\mathbf{r}) = [-\iota v_{\text{F}}\boldsymbol{\alpha}_{\mu\nu} \cdot \boldsymbol{\nabla} + \mathcal{U}(|\mathbf{r}|)\delta_{\mu\nu}]\Psi_\nu(\mathbf{r}) = \delta_{\mu\nu}E\Psi_\nu(\mathbf{r}), \quad (1)$$

where the repeated greek indices are summed over the 4 spinor components of the single-particle Dirac wavefunction. In particular, we are interested in the special case of a potential well/plateau, such that  $\mathcal{U}(|\mathbf{r}| < b) = \lambda$  and  $\mathcal{U}(|\mathbf{r}| \geq b) = \lambda$ .

The first technical step towards solving Eq. (1) is to use a spherical coordinate system —  $(r, \theta, \varphi)$  — and achieve a separation of variables. The way to do it is well-known in relativistic quantum mechanical literature and is based on identifying the orbital and spin angular momentum operators for this system, which read

$$\mathbf{L} = \iota\mathbb{I}_{4 \times 4}\varepsilon^{ijk}x_j\frac{\partial}{\partial x_k} \quad \text{and} \quad \mathbf{S} = \frac{1}{2} \begin{pmatrix} \sigma^i & \mathbb{O}_{2 \times 2} \\ \mathbb{O}_{2 \times 2} & \sigma^i \end{pmatrix}, \quad (2)$$

where the matrices act in the Dirac spinor indices. These quantities are not conserved by the Hamiltonian  $\mathcal{H}$ , however we can build three mutually commuting observables out of  $\mathbf{L}$  and  $\mathbf{S}$ , which are conserved and uniquely define the spinor and angular structure of the eigenfunctions of  $\mathcal{H}$ . These are

$$J_z = \begin{pmatrix} L_z + \frac{1}{2}\sigma^z & \mathbb{O}_{2 \times 2} \\ \mathbb{O}_{2 \times 2} & L_z + \frac{1}{2}\sigma^z \end{pmatrix} \quad \text{and} \quad |\mathbf{J}|^2 = |\mathbf{L} + \mathbf{S}|^2 = \begin{pmatrix} |\mathbf{L}|^2 + \frac{3}{4} + \sigma^i L_i & \mathbb{O}_{2 \times 2} \\ \mathbb{O}_{2 \times 2} & |\mathbf{L}|^2 + \frac{3}{4} + \sigma^i L_i \end{pmatrix} \quad (3a)$$

and also  $\mathcal{K} = \gamma^0 \cdot (2L_i S_i - 1)$ , which explicitly reads

$$\mathcal{K} = \begin{pmatrix} \sigma^i L_i + \mathbb{I}_{2 \times 2} & \mathbb{O}_{2 \times 2} \\ \mathbb{O}_{2 \times 2} & -\sigma^i L_i - \mathbb{I}_{2 \times 2} \end{pmatrix}. \quad (3b)$$

It is easy to verify that all three operators in Eq. (3a) commute among themselves and also with  $\mathcal{H}$ . Crucial for the latter is the fact that  $\mathcal{U}(\mathbf{r}) = \mathcal{U}(r)$ , which guarantees that the impurity does not break rotational symmetry around its center. Therefore, a common eigenbasis of  $|\mathbf{J}|^2$ ,  $J_z$  and  $\mathcal{K}$  can be built and labeled by the good quantum numbers  $j \in \{1/2, 3/2, \dots\}$ ,  $j_z \in \{-j, -j+1, \dots, j\}$  and  $\kappa = \pm 1$ . The number  $\kappa$  appears by solving  $\mathcal{K}$ 's eigenvalue problem,

$$\mathcal{K}\Psi_{j,j_z}(\mathbf{r}) = \hbar^2\kappa \left(j + \frac{1}{2}\right) \Psi_{j,j_z}(\mathbf{r}). \quad (4)$$

Using the previous operators, a general form for the eigenspinors indexed by the set  $(j, j_z, \kappa)$  is

$$\Psi_{j,j_z}^\kappa(r, \theta, \varphi) = \frac{1}{r} \begin{pmatrix} f_j^\kappa(r) \Theta_{j,j_z}^{-\kappa}(\theta, \varphi) \\ \iota g_j^\kappa(r) \Theta_{j,j_z}^\kappa(\theta, \varphi) \end{pmatrix}, \quad (5)$$

where  $f_j^\kappa(r)/g_j^\kappa(r)$  are radial functions and  $\Theta^\kappa(\theta, \varphi)$  are spin-1/2 spherical harmonics,

$$\Theta_{j,j_z}^+(\theta, \varphi) = \begin{pmatrix} \sqrt{\frac{j-j_z+1}{2j+2}} Y_{j_z-1/2}^{j+1/2}(\theta, \varphi) \\ -\sqrt{\frac{j+j_z+1}{2j+2}} Y_{j_z+1/2}^{j+1/2}(\theta, \varphi) \end{pmatrix} \quad \text{and} \quad \Theta_{j,j_z}^-(\theta, \varphi) = \begin{pmatrix} \sqrt{\frac{j+j_z}{2j}} Y_{j_z-1/2}^{j-1/2}(\theta, \varphi) \\ \sqrt{\frac{j-j_z}{2j}} Y_{j_z+1/2}^{j-1/2}(\theta, \varphi) \end{pmatrix}, \quad (6)$$

which in this form are orthonormalized in the unit sphere, i.e.,

$$\int_0^\pi \sin\theta d\theta \int_0^{2\pi} d\varphi [\Theta_{j,j_z}^\kappa(\theta, \varphi)]^\dagger \cdot \Theta_{j',j'_z}^{\kappa'}(\theta, \varphi) = \delta_{j,j'} \delta_{j_z,j'_z} \delta_{\kappa,\kappa'}. \quad (7)$$

Besides the orthonormality condition of Eq. (7),  $\Theta_{j,j_z}^\kappa(\Omega)$  have some further but useful properties, namely,

$$\boldsymbol{\sigma} \cdot \hat{\mathbf{r}} \Theta^\kappa(\theta, \varphi) = (\boldsymbol{\sigma} \cdot \hat{\mathbf{r}})^2 \Theta^\kappa(\theta, \varphi) = \Theta^{-\kappa}(\theta, \varphi) \quad (8a)$$

$$\boldsymbol{\sigma} \cdot \mathbf{L} \Theta^+(\theta, \varphi) = -\hbar \left( j + \frac{3}{2} \right) \Theta^+(\theta, \varphi) \quad (8b)$$

$$\boldsymbol{\sigma} \cdot \mathbf{L} \Theta^-(\theta, \varphi) = \hbar \left( j - \frac{1}{2} \right) \Theta^-(\theta, \varphi), \quad (8c)$$

where  $\boldsymbol{\sigma} = (\sigma^x, \sigma^y, \sigma^z)$  is a vector of Pauli matrices and the scalar products are to be understood as a summation over spacial indices. Finally, we can proceed and write the Hamiltonian  $\mathcal{H}$  explicitly as a differential operator in spherical coordinates. That way, it reads

$$\mathcal{H} = \begin{pmatrix} \mathcal{U}(r) \mathbb{I}_{2 \times 2} & -\nu v_F \boldsymbol{\sigma} \cdot \hat{\mathbf{r}} \left[ \partial_r - \frac{\boldsymbol{\sigma} \cdot \mathbf{L}}{r} \right] \\ -\nu v_F \boldsymbol{\sigma} \cdot \hat{\mathbf{r}} \left[ \partial_r - \frac{\boldsymbol{\sigma} \cdot \mathbf{L}}{r} \right] & \mathcal{U}(r) \mathbb{I}_{2 \times 2} \end{pmatrix}. \quad (9)$$

Using the previous form for  $\mathcal{H}$ , one can plug spinors as in Eq. (5) into the eigenvalue problem of Eq. (1) and get

$$\begin{pmatrix} \mathcal{U}(r) \mathbb{I}_{2 \times 2} & -\nu v_F \boldsymbol{\sigma} \cdot \hat{\mathbf{r}} \left[ \partial_r - \frac{\boldsymbol{\sigma} \cdot \mathbf{L}}{r} \right] \\ -\nu v_F \boldsymbol{\sigma} \cdot \hat{\mathbf{r}} \left[ \partial_r - \frac{\boldsymbol{\sigma} \cdot \mathbf{L}}{r} \right] & \mathcal{U}(r) \mathbb{I}_{2 \times 2} \end{pmatrix} \cdot \begin{pmatrix} \frac{1}{r} f_j^\kappa(r) \Theta_{j,j_z}^{-\kappa}(\theta, \varphi) \\ \frac{i}{r} g_j^\kappa(r) \Theta_{j,j_z}^\kappa(\theta, \varphi) \end{pmatrix} = \frac{E}{r} \begin{pmatrix} f_j^\kappa(r) \Theta_{j,j_z}^{-\kappa}(\theta, \varphi) \\ i g_j^\kappa(r) \Theta_{j,j_z}^\kappa(\theta, \varphi) \end{pmatrix}, \quad (10)$$

which is equivalent to the following coupled systems of ordinary differential equations:

$$\begin{cases} \frac{d}{dr} g_{j,E}^\kappa(r) \pm \frac{1}{r} \left( j + \frac{1}{2} \right) g_{j,E}^\kappa(r) = \frac{1}{v_F} (E - \mathcal{U}(r)) f_{j,E}^\kappa(r) \\ \frac{d}{dr} f_{j,E}^\kappa(r) \mp \frac{1}{r} \left( j + \frac{1}{2} \right) f_{j,E}^\kappa(r) = -\frac{1}{v_F} (E - \mathcal{U}(r)) g_{j,E}^\kappa(r) \end{cases}. \quad (11)$$

In the case of the spherical well/plateau that concerns us, Eq. (11) reduces to either

$$\begin{cases} \frac{d}{dx} g_{j,\varepsilon}^\kappa(x) \pm \frac{1}{x} \left( j + \frac{1}{2} \right) g_{j,\varepsilon}^\kappa(x) = (\varepsilon - u) f_{j,\varepsilon}^\kappa(x) \\ \frac{d}{dx} f_{j,\varepsilon}^\kappa(x) \mp \frac{1}{x} \left( j + \frac{1}{2} \right) f_{j,\varepsilon}^\kappa(x) = -(\varepsilon - u) g_{j,\varepsilon}^\kappa(x) \end{cases}, \quad (12)$$

inside the impurity, or

$$\begin{cases} \frac{d}{dx} g_{j,\varepsilon}^\kappa(x) \pm \frac{1}{x} \left( j + \frac{1}{2} \right) g_{j,\varepsilon}^\kappa(x) = \varepsilon f_{j,\varepsilon}^\kappa(x) \\ \frac{d}{dx} f_{j,\varepsilon}^\kappa(x) \mp \frac{1}{x} \left( j + \frac{1}{2} \right) f_{j,\varepsilon}^\kappa(x) = -\varepsilon g_{j,\varepsilon}^\kappa(x) \end{cases}, \quad (13)$$

outside of it. In Eqs. (12) and (13), we use dimensionless scales, namely —  $x = r/b$ ,  $\varepsilon = Eb/v_F$  and  $u = \lambda b/v_F$ . The solutions inside the impurity (as long as  $\varepsilon \neq u$ ) always have the general form

$$g_{j,\varepsilon}^+(x < 1) = \mathcal{A}^+ \sqrt{x} J_{j+1}(|\varepsilon - u|x) \text{ and } f_{j,\varepsilon}^+(x < 1) = -\mathcal{A}^+ \text{sign}(\varepsilon - u) \sqrt{x} J_j(|\varepsilon - u|x), \quad (14a)$$

$$g_{j,\varepsilon}^-(x < 1) = \mathcal{A}^- \text{sign}(\varepsilon - u) \sqrt{x} J_j(|\varepsilon - u|x) \text{ and } f_{j,\varepsilon}^-(x < 1) = \mathcal{A}^- \sqrt{x} J_{j+1}(|\varepsilon - u|x), \quad (14b)$$

where  $\mathcal{A}^\pm$  are complex adjustable constants. Outside the impurity and for non-zero energy, one has instead

$$g_{j,\varepsilon}^+(x > 1) = \mathcal{B}^+ \sqrt{x} [\cos \delta_j^+(\varepsilon) J_{j+1}(|\varepsilon|x) - \text{sign}(\varepsilon) \sin \delta_j^+(\varepsilon) Y_{j+1}(|\varepsilon|x)] \quad (15a)$$

$$f_{j,\varepsilon}^+(x > 1) = \mathcal{B}^+ \sqrt{x} [\text{sign}(\varepsilon) \cos \delta_j^+(\varepsilon) J_j(|\varepsilon|x) - \sin \delta_j^+(\varepsilon) Y_j(|\varepsilon|x)] \quad (15b)$$

$$g_{j,\varepsilon}^-(x > 1) = \mathcal{B}^- \sqrt{x} [\cos \delta_j^-(\varepsilon) J_{j+1}(|\varepsilon|x) - \text{sign}(\varepsilon) \sin \delta_j^-(\varepsilon) Y_{j+1}(|\varepsilon|x)] \quad (15c)$$

$$f_{j,\varepsilon}^-(x > 1) = -\mathcal{B}^- \sqrt{x} [\text{sign}(\varepsilon) \cos \delta_j^-(\varepsilon) J_j(|\varepsilon|x) - \sin \delta_j^-(\varepsilon) Y_j(|\varepsilon|x)], \quad (15d)$$

where the choice of parameterization in the linear combination was made for convenience. Note that the exterior solutions always have both  $J_n$  and  $Y_n$  components which are always regular and physically admissible in their support ( $x \geq 1$ ). Now, all we must do is to constrain the functions  $\delta_j^\pm(\varepsilon)$  such that the spinor  $\Psi(\mathbf{r})$  is continuous at the impurity's surface ( $x = 1$ ). Using Eqs. (14a)-(15d), this implies that

$$\tan \delta_j^\pm(\varepsilon, u) = \frac{\text{sign}(\varepsilon - u) J_{j+1}(|\varepsilon|) J_j(|\varepsilon - u|) - \text{sign}(\varepsilon) J_j(|\varepsilon|) J_{j+1}(|\varepsilon - u|)}{\text{sign}(\varepsilon) \text{sign}(\varepsilon - u) Y_{j+1}(|\varepsilon|) J_j(|\varepsilon - u|) - Y_j(|\varepsilon|) J_{j+1}(|\varepsilon - u|)}. \quad (16)$$

This equation is independent of  $\kappa$ , which allows us to define a unique function —  $\delta_j(\varepsilon, u)$  — for both the  $\kappa = \pm$  sectors, which appears a single two-fold degeneracy of the states in the problem. The previous facts justify Eq. (4) fo the main text.

The previous analysis is valid for the entire spectrum, except at important  $\varepsilon = 0$  point. Here the interior solutions are the same, but the radial system outside the impurity decouples, i.e.

$$\begin{cases} \frac{d}{dx} g_{j,\varepsilon}^\kappa(x) \pm \frac{1}{x} (j + \frac{1}{2}) g_{j,\varepsilon}^\kappa(x) = 0 \\ \frac{d}{dx} f_{j,\varepsilon}^\kappa(x) \mp \frac{1}{x} (j + \frac{1}{2}) f_{j,\varepsilon}^\kappa(x) = 0 \end{cases} . \quad (17)$$

The latter allows for power-law solutions, of which the physically admissible (i.e., the ones decaying with  $x$ ) are of the form

$$g_{j,\varepsilon=0}^+(x \geq 1) = \frac{\mathcal{B}^+}{x^{j+1/2}} \text{ and } f_{j,\varepsilon=0}^+(x \geq 1) = 0 \quad (18a)$$

$$g_{j,\varepsilon=0}^-(x \geq 1) = 0 \text{ and } f_{j,\varepsilon=0}^-(x \geq 1) = \frac{\mathcal{B}^-}{x^{j+1/2}}. \quad (18b)$$

Both these solutions, being joined continuously to the interior solutions of Eqs. (14a) and (14b) require that  $J_j(|u|) = 0$ . This condition gives rise to a discrete set of parameters  $u$ , for which these bound-state solutions are allowed.

Finally, we remark that all the eigenstates determined here (the unbound and bound ones) have an intrinsic  $2j + 1$  degeneracy due to the rotation invariance of the Hamiltonian. This degeneracy factor is explicitly taken into account in all calculations done in the main text.

#### *b. Self-Adjoint Restriction of the Dirac Hamiltonian to a Finite Sphere*

In our derivation of the relation between the scattering phase shifts and the change in the DoS due to a dilute diversity of impurities, we make an explicit use of the restriction of  $\mathcal{H}$  to a finite sphere of radius  $R \gg b$  —  $S_R$ . Restricting a continuum Hamiltonian to a finite volume of space generally makes its action on the original Hilbert space non-hermitian. The way around this is to impose appropriate boundary conditions which restrict the original basis to a subset, generating a subspace inside of which the Hamiltonian preserves its hermiticity. This is called taking a self-adjoint extension of  $\mathcal{H}$  to a finite domain.

In the case of the Dirac hamiltonian with a scalar potential —  $\mathcal{H} = -\nu_F \boldsymbol{\alpha} \cdot \nabla + \mathcal{U}(\mathbf{r})$  — the hermiticity condition is imposed by guaranteeing that, for any two Dirac spinor states  $\Phi^1(\mathbf{r})$  and  $\Phi^2(\mathbf{r})$ , the following condition holds:

$$\int_{S_R} d^3\mathbf{r} [\Phi_\mu^2(\mathbf{r})]^\dagger [-\nu_F \boldsymbol{\alpha}_{\mu\nu} \cdot \nabla + \mathcal{U}(\mathbf{r}) \delta_{\mu\nu}] \Phi_\nu^1(\mathbf{r}) = \left[ \int_{S_R} d^3\mathbf{r} [\Phi_\mu^1(\mathbf{r})]^\dagger [-\nu_F \boldsymbol{\alpha}_{\mu\nu} \cdot \nabla + \mathcal{U}(\mathbf{r}) \delta_{\mu\nu}] \Phi_\nu^2(\mathbf{r}) \right]^* . \quad (19)$$

After some straightforward manipulation, this condition can be cast into the equivalent form

$$\oint_{\partial S_R} d^2S [\Phi_\mu^1(\mathbf{r})]^\dagger [\boldsymbol{\alpha}_{\mu\nu} \cdot \hat{\mathbf{n}}] \Phi_\nu^2(\mathbf{r}) = 0, \quad (20)$$

where  $\hat{\mathbf{n}} = (n_x, n_y, n_z)$  is an outwards unit vector normal to the spherical surface  $\partial S_R$ . This is precisely the condition presented in the main text. Unsurprisingly, Eq. (20) is easily interpreted as guaranteeing that no net particle current crosses the boundary of  $S_R$ , which expresses particle conservation implied by hermiticity.

Meanwhile, since all  $\boldsymbol{\alpha}$  matrices are composed of off-diagonal  $2 \times 2$  blocks, one can easily see that Eq. (20) is satisfied whenever we impose either the first or the last two components of the Dirac spinors to be zero at  $\partial S_R$ . Considering spinors of the form given in Eq. (5), such condition translates into either  $f_j^+(R) = g_j^-(R) = 0$  or  $f_j^-(R) = g_j^+(R) = 0$ . The other two combinations cannot be satisfied, as the zeros of Bessel functions of different  $j$ 's never coincide. For the purposes of this work, we chose the first of these conditions (although the specific self-adjoint extension should not be relevant for any thermodynamic limit results). Finally, by using the general form of the exterior scattering solutions found earlier [Eqs. (15a)-(15d)], we arrive at our final form for the boundary condition,

$$\cos \delta_j(\varepsilon, u) J_j(|\varepsilon| R) - \text{sign}(\varepsilon) \sin \delta_j(\varepsilon) Y_j(|\varepsilon| R) = 0, \quad (21)$$

where  $R$  is measured in units of  $b$ .

Before proceeding, we remark about an important consequence of the boundary condition in Eq. (21). For a start, this condition imposes a quantization of energy levels, turning the continuous spectrum into a discrete one with a density of levels that scales with  $R$ . Provided that we are looking at finite energies ( $\varepsilon \neq 0$ ) and with  $|\varepsilon|R \gg 1$ , Eq. (21) can be taken in its asymptotic form, namely,

$$\cos\left(|\varepsilon|R + \frac{\pi}{2}\left(j + \frac{1}{2}\right) + \text{sign}(\varepsilon)\delta_j(\varepsilon, u)\right) = 0. \quad (22)$$

In the absence of an impurity, we have  $\delta_j(\varepsilon, 0) = 0$  and the mesh of energy levels allowed by the boundary conditions (in a given  $j$ -sector) is simply  $-\varepsilon_n^j \approx \frac{n\pi}{R} + \text{sign}(n)\frac{\pi}{2R}(j + 1/2)$  with  $n \in \mathbb{Z}$  and provided  $R$  is large enough. This yields a mean-level spacing which is uniform across the spectrum and equal to  $\pi R^{-1}$ . In the presence of the impurity (which induces energy dependent phase-shift), Eq. (22) does not seem to have a simple solution. However, if  $R$  is large enough such that  $\delta_j(\varepsilon, u)$  is a slowly varying function across an energy interval of width  $\pi R^{-1}$ , then one can say that the allowed energy levels are roughly

$$\varepsilon_n^j \approx \frac{n\pi}{R} + \text{sign}(n)\frac{\pi}{2R}(j + 1/2) - \frac{\delta_j(\varepsilon_n^j, u)}{R},$$

which gives a correction to the mean-level spacing relative to the case  $u = 0$ , which is simply

$$\varepsilon_{n+1}^j - \varepsilon_n^j \approx \frac{\pi}{R} - \frac{1}{R}\left[\delta_j\left(\varepsilon_n^j + \frac{\pi}{R}, u\right) - \delta_j\left(\varepsilon_n^j, u\right)\right] \approx \frac{\pi}{R}\left[1 - \frac{\pi}{R}\frac{\partial}{\partial\varepsilon}\delta_j(\varepsilon, u)\Big|_{\varepsilon=\varepsilon_n^j}\right],$$

with an analogous expression for  $n < 0$ . Hence, we conclude that the correction to the mean-level spacing due to a single impurity is always  $\propto \mathcal{O}(R^{-2})$ , which is sub-leading relative to the original  $\pi/R$  spacing. This result is exemplified by a numerical solution of Eq. (21) in Fig. 1, and justifies our arguments on the number of states migrating in/out an energy interval given in the main text.

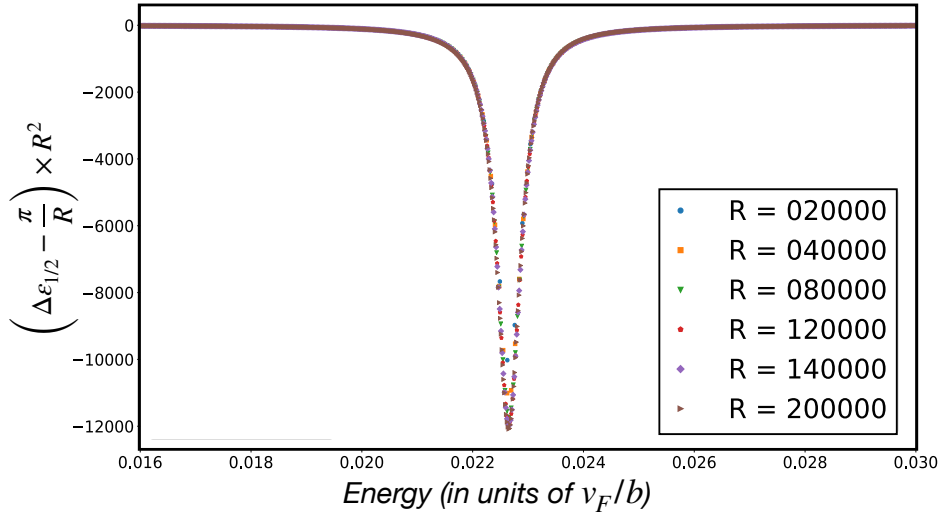


Figure 1. Plot of  $\Delta\varepsilon_{1/2} = \varepsilon_{n+1}^{1/2} - \varepsilon_n^{1/2}$  the nearest-level spacings for a spherical impurity with  $u = 3.1867$  calculated from the numerically found solutions of the boundary condition [Eq. (21)]. The data points are represented as  $R^2 \times (\Delta\varepsilon_{1/2} - \pi R^{-1})$ , such that a collapse of different values of  $R$  is achieved. This collapse indicates that  $\Delta\varepsilon_{1/2}(R, \varepsilon, u) \approx \pi R^{-1} - f(\varepsilon, u)R^{-2}$  in the presence of an impurity.  $R$  is measured in units of  $b$ .

## 2. A Consistent Definition of the Scattering Phase Shifts

In this section, we use the spherical Dirac eigenstates found earlier to define the scattering phase shifts in a way that allows a direct relation to the impurity induced change in the density of states. We recover early results which explain the crucial zero-energy  $\pi$ -discontinuity observed in our calculations as due to the appearance of critical bound states in the transition between the valence and conduction band. This connects our results to *Levinson's Theorem* applied to noninteracting Dirac particles.

The exterior scattering wavefunctions of the gapless Dirac equation with a spherical well/plateau (of strength  $\lambda$  and radius  $b$ ) were found to be of the form

$$\Psi_{E,j,j_z}^+(r, \Omega) = \mathcal{N}^+ \begin{pmatrix} [\cos \delta_j(E, \lambda b) J_j(|E|r) - \text{sign}(E) \sin \delta_j(E, \lambda b) Y_j(|E|r)] \Theta_{j,j_z}^-(\Omega) \\ \iota [\cos \delta_j(E, \lambda b) J_{j+1}(|E|r) - \text{sign}(E) \sin \delta_j(E, \lambda b) Y_{j+1}(|E|r)] \Theta_{j,j_z}^+(\Omega) \end{pmatrix} \quad (23)$$

and

$$\Psi_{E,j,j_z}^-(r, \Omega) = \mathcal{N}^- \begin{pmatrix} [\cos \delta_j(E, \lambda b) J_{j+1}(|E|r) - \text{sign}(E) \sin \delta_j(E, \lambda b) Y_{j+1}(|E|r)] \Theta_{j,j_z}^+(\Omega) \\ -\iota [\cos \delta_j(E, \lambda b) J_j(|E|r) - \text{sign}(E) \sin \delta_j(E, \lambda b) Y_j(|E|r)] \Theta_{j,j_z}^-(\Omega) \end{pmatrix}, \quad (24)$$

where  $\mathcal{N}^\pm$  are complex normalization constants and  $\delta_j(E, \lambda b)$  are the energy-dependent scattering phase-shifts. From the forms of Eqs. (23)-(24), it is clear that summing  $n \times \pi$  (with integer  $n$ ) to the phase-shifts yields exactly the same spinor states, apart from irrelevant global sign changes. Meanwhile, the scattering phase-shifts must always obey

$$\tan \delta_j(\varepsilon, u) = \frac{\text{sign}(\varepsilon) J_j(|\varepsilon|) J_{j+1}(|\varepsilon - u|) - \text{sign}(\varepsilon - u) J_{j+1}(|\varepsilon|) J_j(|\varepsilon - u|)}{Y_j(|\varepsilon|) J_{j+1}(|\varepsilon - u|) - \text{sign}(\varepsilon) \text{sign}(\varepsilon - u) Y_{j+1}(|\varepsilon|) J_j(|\varepsilon - u|)}, \quad (25)$$

where  $\varepsilon = Eb/\hbar v_F$  and  $u = \lambda b/\hbar v_F$ . It is this condition that guarantees continuity of the wavefunctions at  $r = b$ . However, as explained in the main text, this condition does not uniquely define the functions  $\delta_j(\varepsilon, u)$  and a choice must be made concerning the reference situation relative to which the wavefunctions get dephased.

A natural choice is to define  $\delta_j$  as the phase shift of the wavefunction relative to the case when  $u = 0$ . More precisely, we can think of a situation in which the central potential is adiabatically turned on and the instantaneous scattering eigenstates get progressively more dephased at all energies. This convention is known to be a useful one for Dirac fermions [41, 42] and it can be achieved by enforcing  $\delta_j(\varepsilon \rightarrow \pm\infty, u) \rightarrow -u$ . It is important to remark that this choice is needed for us to relate the change in the number of states inside a fixed spectral window with the phase shifts of scattering states in that window. In Fig. 2, we depict the lowest- $j$  phase shifts,  $\delta_{1/2}(\varepsilon, u)$  and  $\delta_{3/2}(\varepsilon, u)$ , as a function of energy when  $u$  is close to a critical value. Those curves were obtained using the previous convention for the phase shifts ( $\delta_j(\varepsilon \rightarrow \pm\infty, u) \rightarrow -u$ ), which can be guaranteed by the following numerical integration:

$$\delta_j(\varepsilon, u) = \begin{cases} -u + \int_{-\infty}^{\varepsilon} dx \frac{d}{dx} \arctan \left[ \frac{\text{sign}(x) J_j(|x|) J_{j+1}(|x-u|) - \text{sign}(x-u) J_{j+1}(|x|) J_j(|x-u|)}{Y_j(|x|) J_{j+1}(|x-u|) - \text{sign}(x) \text{sign}(x-u) Y_{j+1}(|x|) J_j(|x-u|)} \right] & \text{if } \varepsilon < 0 \\ -u + \int_{\infty}^{\varepsilon} dx \frac{d}{dx} \arctan \left[ \frac{\text{sign}(x) J_j(|x|) J_{j+1}(|x-u|) - \text{sign}(x-u) J_{j+1}(|x|) J_j(|x-u|)}{Y_j(|x|) J_{j+1}(|x-u|) - \text{sign}(x) \text{sign}(x-u) Y_{j+1}(|x|) J_j(|x-u|)} \right] & \text{if } \varepsilon \geq 0 \end{cases}. \quad (26)$$

Defining  $\delta_j$  by branches guarantees not only that the appropriate asymptotic convention is obeyed but also that the discontinuity due to zero-energy bound-states is always avoided in the integrals.

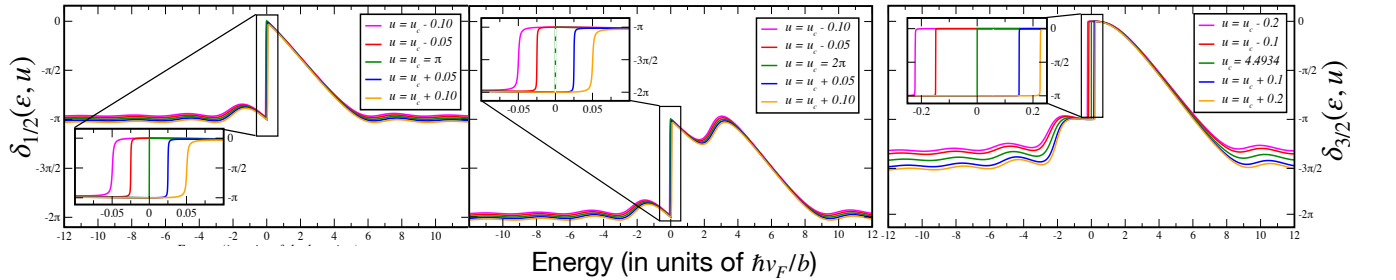


Figure 2. Plots of the phase shifts for  $j = 1/2$  (left and middle panels) around the two first critical values  $u = \pi, 2\pi\hbar v_F a^{-1}$ , and the first critical value  $u \approx 4.4934 \dots$  for  $j = 3/2$ . The main panels show the assigned asymptotic behavior  $-\delta_j(\varepsilon \rightarrow \pm\infty, u) \rightarrow -u$  in each case, while the insets depict the formation of a true  $\pi$ -discontinuity at  $\varepsilon = 0$  when  $u = u_c^j$ .

Finally, from Fig. 2 it is clear that a  $\pi$ -discontinuity develops at  $\varepsilon = 0$  when the impurity parameter is critical. This is the trademark of a zero-energy bound-state since. According to *Levinson's theorem* for gapless Dirac particles, the number of bound-states with well-defined  $j, j_z$  and  $\kappa$  is given as (see Ma and Ni [41])

$$n_{j,j_z,\kappa=\pm}(u) = \frac{1}{\pi} [\delta_j^\pm(0^+, u) + \delta_j^\pm(0^-, u)] \mp \frac{(-1)^{j+1/2}}{2} [\sin^2 \delta_j^\pm(0^+, u) - \sin^2 \delta_j^\pm(0^-, u)], \quad (27)$$

which yields  $n_{j,j_z,\kappa=\pm}(u \neq n_c^j) = 0$  and  $n_{j,j_z,\kappa=\pm}(u = n_c^j) = 1$ . This agrees with our earlier derivation of the zero-energy eigenstates in this system.

### 3. Additional Numerical Results and Technical Details

#### a. Technical Description of the Numerical Method

Here, we provide some technical details on the numerical method used for calculating the density of states in the lattice model defined in Eq. (7) of the main text. As explained there, the calculations used a kernel polynomial method [48], implemented in an efficient CPU parallelized framework developed by some of us (Quantum Kite [47]). We begin by outlining the basic elements of our numerical method.

Our aim is to calculate the intensive density of states (DoS) of a finite quantum lattice system with  $N$  degrees of freedom (in our case,  $N = 4L^3$ , as we have a simple cubic lattice with side  $L$  and 4 orbitals per site). This quantity is given generically as  $\rho(\varepsilon) d\varepsilon = \frac{1}{N} \sum_{\alpha} g_{\alpha} \delta(\varepsilon - \varepsilon_{\alpha}) d\varepsilon$ , where the summation is over eigenvalues of  $\mathcal{H}$  and  $g_{\alpha}$  is the degeneracy of each level. For our numerical purposes,  $\rho(\varepsilon) d\varepsilon$  is expanded in Chebyshev polynomials of the 1<sup>st</sup>-kind,  $T_n(x)$ , yielding

$$\rho_{\text{KPM}}(\varepsilon, M) d\varepsilon = \left\{ \frac{1}{\pi\sqrt{\lambda^2 - \varepsilon^2}} + 2 \sum_{n=1}^M \frac{g_n^J(M) T_n(\varepsilon/\lambda)}{\pi\sqrt{\lambda^2 - \varepsilon^2}} \text{Tr} \left[ T_n(\tilde{\mathcal{H}}) \right] \right\} d\varepsilon, \quad (28)$$

where  $M$  is a truncation order,  $\tilde{\mathcal{H}} = \mathcal{H}/\lambda$  is a rescaled Hamiltonian with spectrum contained inside the interval  $[-1, 1]$  and  $\tilde{\varepsilon} = \varepsilon/\lambda$  is a rescaled energy. Also,  $g_n^J(M) = \left[ (M - n + 1) \cos\left(\frac{\pi n}{M+1}\right) + \cot\left(\frac{\pi}{M+1}\right) \sin\left(\frac{\pi n}{M+1}\right) \right] / [M + 1]$  is the so-called Jackson kernel which effectively damps the Gibbs oscillations in the truncated approximation. This method introduces a finite spectral resolution in the calculation which, near the band center, is  $\eta(M) \approx \pi\lambda/M$ . The resolution becomes narrower by increasing  $M$ .

Finally, we remark that given a function  $f(x)$  which is approximated with a finite resolution in  $x$ , the KPM-approximated function is described as the following convolution integral:

$$f_{\text{KPM}}(x, \eta) = \int_{-1}^1 d\tau f(x) \frac{e^{-\frac{(x-\tau)^2}{2\eta^2}}}{\sqrt{2\pi}\eta}. \quad (29)$$

This result is used for most of the analysis done on our real-space numerical results.

#### b. Lattice Model and Boundary Conditions

In this brief section, we provide details and illustrate the lattice model used in all our numerical simulations. As referred in the main text, our basic lattice Hamiltonian  $H^{\text{D}}$  was obtained by discretizing the continuum Dirac Hamiltonian (with a scalar potential  $\mathcal{U}(\mathbf{R})$ ) —  $\mathcal{H}^{\text{D}}$  — in a simple cubic lattice with 4 orbitals per site. This tight-binding model Hamiltonian reads

$$H^{\text{D}} = \frac{v_{\text{F}}}{2a} \sum_{\mathbf{R} \in \mathcal{L}_{\text{C}}} \sum_{j=1}^3 \left\{ \Psi_{\mathbf{R}}^{\dagger} \cdot \alpha^j \cdot \Psi_{\mathbf{R}+a\hat{e}_j} - \text{h.c.} \right\} + \sum_{\mathbf{R} \in \mathcal{L}_{\text{C}}} \mathcal{U}(\mathbf{R}) \Psi_{\mathbf{R}}^{\dagger} \cdot \Psi_{\mathbf{R}}, \quad (30)$$

where  $a$  is the lattice parameter and  $\Psi_{\mathbf{R}}^{\dagger} = \left( c_{\mathbf{R},A,\uparrow}^{\dagger}, c_{\mathbf{R},A,\downarrow}^{\dagger}, c_{\mathbf{R},B,\uparrow}^{\dagger}, c_{\mathbf{R},B,\downarrow}^{\dagger} \right)$  is a vector with onsite fermionic creation operators. Here,  $A/B$  stand for two different sublattices while  $\downarrow/\uparrow$  are the two spin states in each orbital. Note that this convention for naming the local single-particle states is consistent with the previously defined intrinsic angular momentum operator,  $\mathbf{S}$ . In Fig. 3a, we depict this real-space model in terms of its hoppings.

In the clear limit,  $\mathcal{U}(\mathbf{R})$ , this lattice model can be diagonalized by going to  $\mathbf{k}$ -space. After doing that we obtain the particle-hole symmetric dispersion relation

$$E^{c/v}(\mathbf{k}) = \pm \frac{v_{\text{F}}}{a} \sqrt{\sin^2 k_x a + \sin^2 k_y a + \sin^2 k_z a}, \quad (31)$$

where both the conduction and valence bands are two-fold degenerate. At half filling, this clearly reproduces a 3D Dirac semimetal, with 8 valleys placed at the time-reversal invariant momenta (TRIM) of the first Brillouin zone. These are shown in Fig. 3b. Near a TRIM,  $\mathbf{K}_{\text{D}}$ , the dispersion relation takes the form

$$E^{c/v}(\mathbf{k}) \approx \pm v_{\text{F}} |\mathbf{k} - \mathbf{K}_{\text{D}}|,$$

which is exactly the same as we had in our original continuum Hamiltonian. Nevertheless, the discretization of  $\mathcal{H}_D$  introduces a replication of the original four-fold degenerate Dirac cone into 8 disconnected ones.

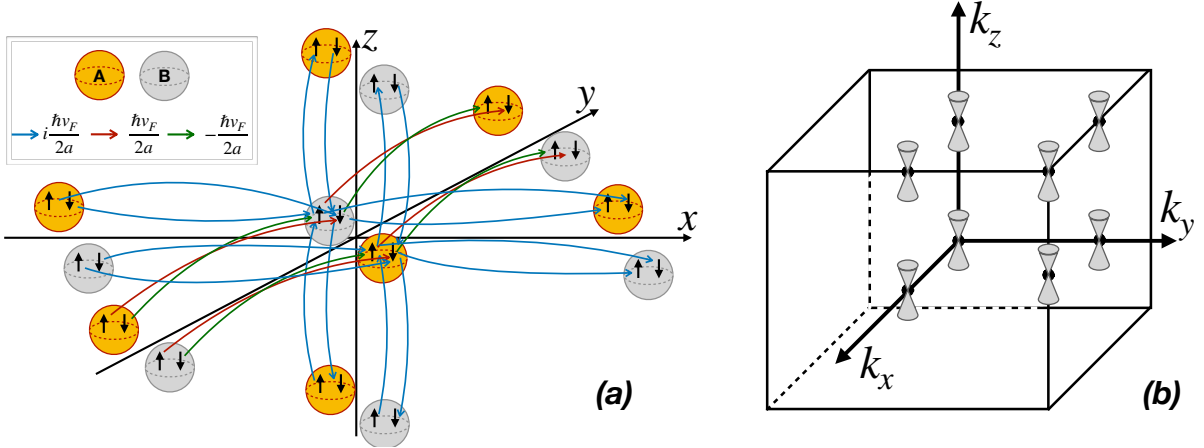


Figure 3. **(a)** Schematic depiction of the nearest-neighbor hoppings in the kinetic part of the Hamiltonian  $H^D$ . Going in the direction inverse to that indicated by the arrows means that the hopping will have the complex conjugate value. **(b)** Representation of the simple cubic first Brillouin zone of the model together with the places where the 8 Dirac nodes are present in the limit  $\mathcal{U}(\mathbf{R}) = 0$ .

Before ending this section, it is useful to calculate the normalized DoS of the clean lattice model, as it is used explicitly in the analysis of our numerical results. Using our previous definition, the intensive DoS for this systems (assuming a simulated lattice with  $L^3$  sites) reads

$$\rho_0(\varepsilon) = \frac{2}{4L^3} \sum_{\mathbf{k} \in \text{FBZ}} \delta\left(\varepsilon \mp \frac{v_F}{a} \sqrt{\sin^2 k_x a + \sin^2 k_y a + \sin^2 k_z a}\right).$$

Due to particle-hole symmetry ( $\varepsilon \rightarrow -\varepsilon$ ), we are entitled to only care about positive energies. Numerically, we can choose a regular mesh in the first Brillouin zone of the cubic lattice (equivalent to choosing a finite real-space cell) and determine the normalized DoS. This is shown in Fig. 4, together with the corresponding low-energy quadratic approximation. The latter is simply  $\rho_0(\varepsilon) = 2\varepsilon^2/\pi^2$ , which is the expression used in the main text.

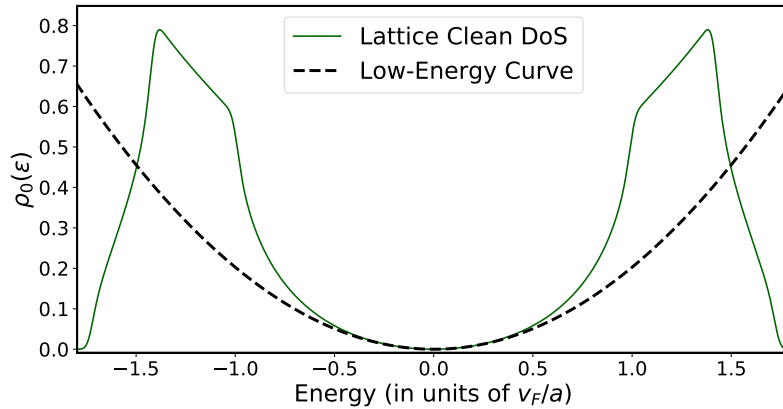


Figure 4. Plot of the normalized density of states calculated for the lattice model of Eq. (30) (green curve). The dashed black curve corresponds to the quadratic low-energy approximation to the DoS —  $\rho_0(\varepsilon) \simeq 2\varepsilon^2/\pi^2$ .

### c. Additional Results for the Resonances of a Single Sphere

In this section, we present additional details on the numerical results presented in the main text, together with additional results supporting our conclusions. We begin by presenting the numerical results for the change in the density of states due to a single extended sphere in the center of a simulated supercell of size  $L^3$ . Despite simulating a single sphere, we are actually sampling over random realizations of boundary phase twists — this known technique helps the convergence of the KPM calculations (by eliminating the mean level spacing from the problem), but corresponds to considering an infinite superlattice by repetition of the simulated cell.

In Fig. 5, we show numerical results for the  $\Delta\rho_{\text{imp}}(E, u)L^3 = (\rho_{\text{imp}}(E, u) - E^2/2\pi^2)L^3$  for values of  $u$  around  $\pi$ , the first positive critical value for a bound-state with  $j = 1/2$ . These results are compared to theoretical curves (dashed black lines), obtained from FSR's result,

$$\Delta\rho_{\text{imp}}^j(E, u) = 8 \frac{2(2j+1)}{4\pi L^3 a^3} \frac{d\delta_j(\varepsilon, u)}{d\varepsilon} \text{ with } \varepsilon = Eb, \quad (32)$$

convoluted with a gaussian —

$$\Delta\tilde{\rho}_{\text{imp}}^j(E, u) = -\frac{2E^2}{\pi^2} + \frac{1}{\sqrt{2\pi}\eta} \int_{-\infty}^{\infty} dx e^{-\frac{(E-x)^2}{2\eta^2}} \left[ \Delta\rho_{\text{imp}}^j(x, u) + \frac{2x^2}{\pi^2} \right] \quad (33)$$

— to account for the finite spectral resolution,  $\eta$ , implied by the numerical method. Note that Eq. (32) includes a factor of 8 which accounts for the eight Dirac valleys existing in our lattice model, as well as a 1/4 due to the four orbitals per site in our lattice model. The numerically calculated DoS is then normalized by the number of states —  $4L^3$  — and the clean system has  $\rho(E) \approx 2E^2/\pi^2$  for  $E \approx 0$ .

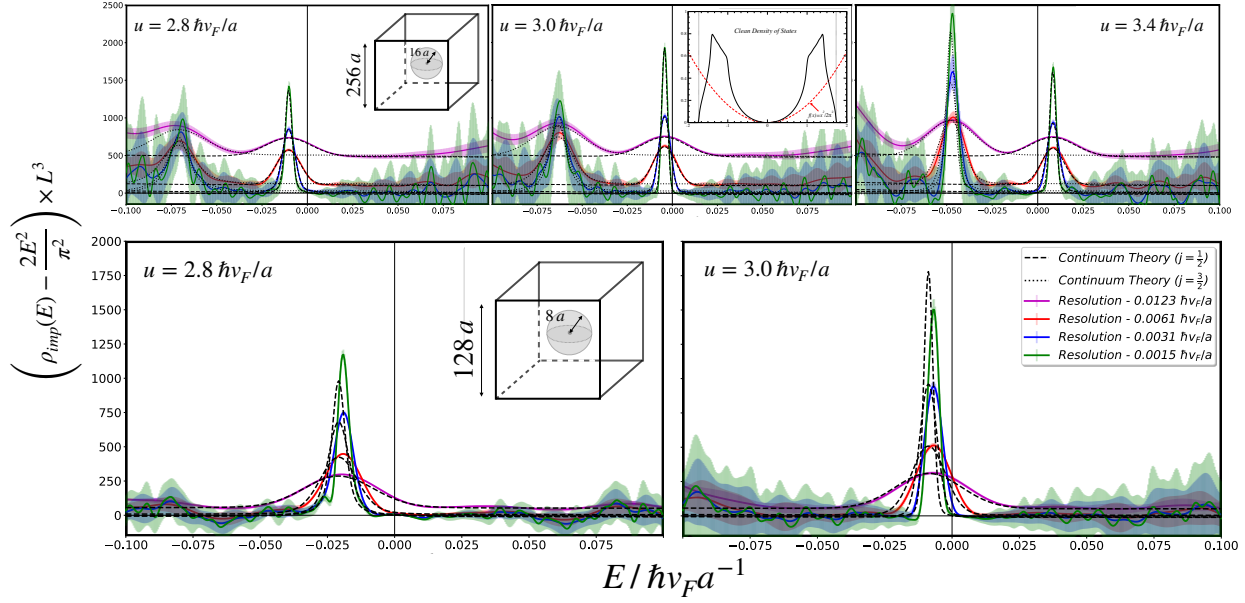


Figure 5. **Upper Panel:** Plots of the change in the density of states due to a single spherical impurity of strength  $u = 2.8, 3.0, 3.4 v_F a^{-1}$  and radius  $b = 16 a$ , inside a simulated supercell of volume  $256^3 a$ . The vertical widths of the numerical curves are 95% statistical error bars, with respect to the simultaneous sampling over random KPM vectors and boundary phase-twists. The agreement with the resolution-corrected theoretical curves is perfect over the entire range of resolutions used. **Lower Panel:** Results for a single spherical impurity of strength  $u = 2.8, 3.0 v_F a^{-1}$  and radius  $b = 8 a$ , inside a simulated supercell of volume  $256^3 a$ . Finite-size effects due to the discretization of the spherical impurity in the lattice are now visible as shift of the peak away from the node.

As can be seen from Fig. 5, the agreement with the curves obtained from the continuum theory is perfect for spheres of radius  $b > 16 a$  with a concentration smaller than  $256^3 a^{-3}$  till energy resolutions of meV. For spheres of radius  $b = 8 a$ , one already observes deviations from the continuum theory curves in the form of energy shifts (see lower panels in Fig. 5).

In Fig. 6, we represent analogous high-energy-resolution numerical results for  $u \approx 4.493 \dots$  corresponding to the first resonance associated to  $j = 3/2$ . In the plots, one can also observe the next resonance (with  $j = 5/2$ ) approaching the Dirac node. One can see that a radius of  $16 a$  is not sufficiently large to have a complete agreement between the numerical peaks and the continuum theoretical curves. In the lower panel, the calculation is repeated for a larger radius of the spherical impurity ( $b = 22 a$ ) and a perfect agreement is then obtained for  $j = 3/2$ .

Finally, it is important to analyze directly the case when the single impurity inside the supercell is at a critical value. In this case, we claim that uncoupled zero-energy eigenstates exist for the configuration, contributing as  $8\delta(E)/L^3$  to the DoS (contributions coming from different valleys, as well as the factor of 4 due to the normalization to the total number of orbitals are included). One can never see such a contribution numerically using the previous procedure, but we can analyze its emergence as a function of the spectral resolution. More precisely, we must have

$$\Delta\tilde{\rho}_{\text{imp}}^j(E, u_c) = -\frac{2E^2}{\pi^2} + \frac{1}{\sqrt{2\pi}\eta} \int_{-\infty}^{\infty} dx e^{-\frac{(E-x)^2}{2\eta^2}} \left[ \frac{8}{L^3} \delta(x) + \frac{2x^2}{\pi^2} \right] = \frac{2\eta^2}{\pi^2} + \frac{8}{\sqrt{2\pi}L^3\eta} e^{-\frac{E^2}{2\eta^2}}, \quad (34)$$

which is compared to numerical results (for  $u = \pi$ ) in Fig. ???. The agreement is perfect.

To close this section, we remark that the main conclusions to be drawn from the previous single-impurity results are three-fold: 1) The continuum theory describes the DoS peaks corresponding to resonances associated to dilute “near-critical” spherical impurities, provided that this peak is located near the Dirac node (where the continuum theory holds), the radius of the spheres is large enough, and the distance between spheres is sufficiently large; 2) Larger- $j$  resonances require the discretized spheres to be larger in order to reproduce the continuum theory results for the same energy resolutions; 3) Numerically, one can observe the emergence of a Dirac- $\delta$  at zero energy when the dilute impurities are all at critical values.

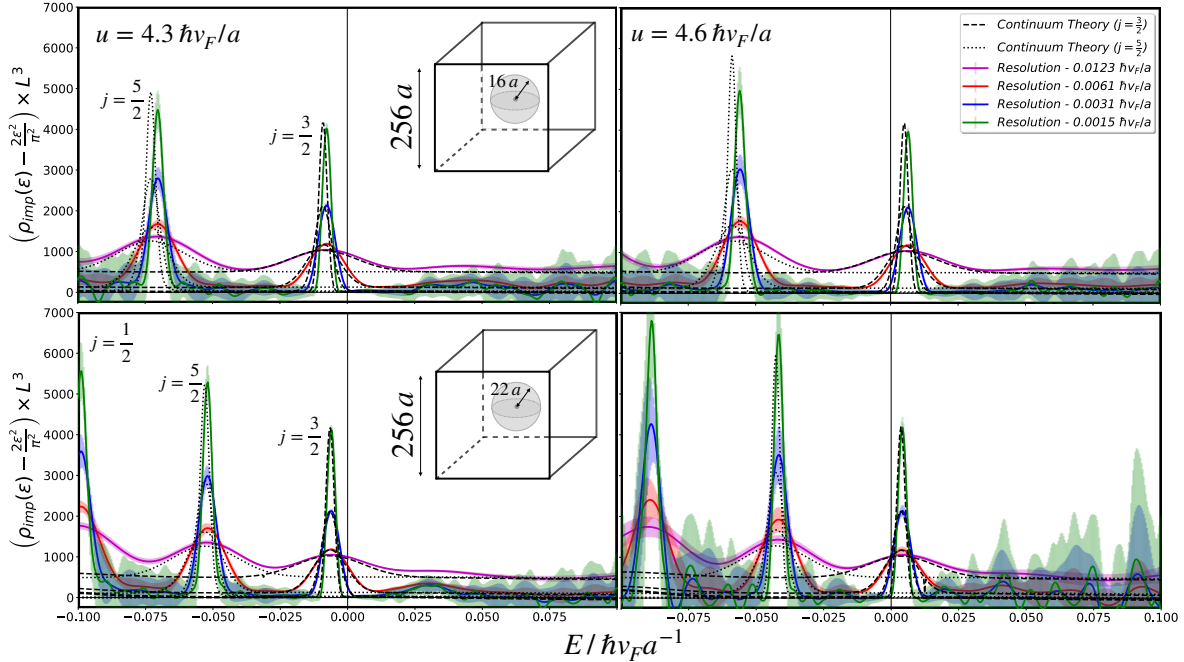


Figure 6. **Upper Panels:** Plots of the change in the density of states due to a single spherical impurity of strength  $u = 4.3, 4.6 v_F a^{-1}$  and radius  $b = 16 a$  inside a simulated supercell of volume  $256^3 a$ . The vertical widths of the numerical curves are 95% statistical error bars. The two visible peaks correspond to the first resonances associated to  $j = 5/2$  and  $j = 3/2$ , from left to right. **Lower Panels:** Same calculations done for an impurity of radius  $b = 22 a$ . The agreement with the continuum theory is much better in this case.

#### d. Details on the Simulation of the Average DoS for a System of Random Impurities

Here, we provide details on the generation of the random distribution of non-overlapping spheres in the lattice used to produce the numerical results of Fig. 4b. In order to do this, we started by considering a simulated supercell (with twisted boundaries) with  $512^3$  unit cells ( $\approx 536$  million orbitals), which from the results of the previous single-impurity simulations is more than enough to reproduce the single sphere  $\Delta\rho(E)$  at low energies if spheres of radius  $16 a$  are considered. Then, we generate the potential associated to a regular cubic lattice composed by the centers of such (discretized) spheres inside the simulated cell. This procedure is equivalent to subdividing the original supercell side by an integer number, generating a set of identical subcells.

Finally, each of the generated central points is randomly displaced in three-dimensional space and a potential strength randomly chosen for each impurity inside the supercell. This procedure guarantees that there are no superpositions in any sample, as one restricts the random displacement of the centers to keep it inside the corresponding subcell. A cartoon for this procedure is depicted in Fig. 7. Once the full potential landscape inside the supercell is created, the remaining numerical procedure is identical to what was previously described.

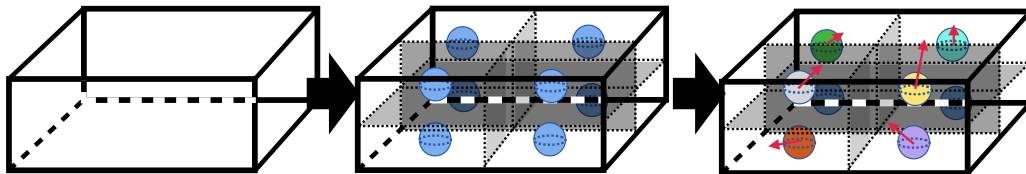


Figure 7. Scheme of the procedure used to generate a configuration of multiple random spheres inside the simulated supercell.